

Recombination coefficients for O II lines in nebular conditions

P.J. Storey¹, Taha Sochi^{1*}, Robert Bastin²

¹*Department of Physics and Astronomy, University College London, Gower Street, London, WC1E 6BT, UK*

²*Surbiton High School, Kingston upon Thames, Greater London, Surrey, KT1 2JT, UK*

Accepted 2017 May 11. Received 2017 May 10; in original form 2017 March 28

ABSTRACT

We present the results of a calculation of recombination coefficients for $O^{2+} + e^{-}$ using an intermediate coupling treatment that fully accounts for the dependence of the distribution of population among the ground levels of O^{2+} on electron density and temperature. The calculation is extended down to low electron temperatures where dielectronic recombination arising from Rydberg states converging on the O^{2+} ground levels is an important process. The data, which consist of emission coefficients for 8889 recombination lines and recombination coefficients for the ground and metastable states of O^{+} are in Cases A, B and C, and are organised as a function of the electron temperature and number density, as well as wavelength. An interactive fortran 77 data server is also provided as an accessory for mining the line emission coefficients and obtaining Lagrange interpolated values for any choice of the two variables between the explicitly provided values for any set of wavelengths. Some illustrations of the application of the new data to nebular observations are also provided.

Key words: atomic data – atomic processes – radiation mechanisms: general – radiation mechanisms: non-thermal – planetary nebulae: general – ISM: H II regions – astrochemistry – plasmas – methods: numerical.

1 INTRODUCTION

O II recombination lines have been observed in the spectra of many planetary nebulae and H II regions (Peimbert *et al* 1993; Liu *et al* 1995; Baldwin *et al* 2000; Garnett & Dinerstein 2001; Wesson *et al* 2003; Esteban *et al* 2004; Wesson *et al* 2005; Robertson-Tessi & Garnett 2005; Peimbert & Peimbert 2005; Liu *et al* 2006; Esteban *et al* 2009; Mesa-Delgado & Esteban 2010; Peimbert & Peimbert 2013; Peimbert *et al* 2014), and hence many of these lines (e.g. $\lambda\lambda 4076, 4089$ and the V1 multiplet) have been used (Liu *et al* 2004; Tsamis *et al* 2004; Wesson *et al* 2005; Bastin 2006; Bastin & Storey 2006; Wang & Liu 2007; McNabb *et al* 2013) as diagnostic tools for probing the physical conditions of the emitting regions.

Regarding previous theoretical and computational work on O^{+} recombination processes, Nussbaumer & Storey (1984) calculated the effective dielectronic recombination coefficients for a number of selected O II recombination lines in an LS -coupling approximation. Péquignot *et al* (1991) calculated total and effective radiative recombination coefficients for several important O II lines and provided them in the form of fitting formulae valid over certain tempera-

ture ranges. Similar calculations were carried out by Smits (1991) for selected lines where the calculations were based on an LS -coupling scheme. The work of Nussbaumer & Storey (1984) was extended by Storey (1994) who computed effective recombination coefficients for a number of O II lines based on a full LS -coupled O^{+} model atom at electron temperatures and number densities relevant to planetary nebulae. Liu *et al* (1995) provided O II radiative recombination coefficients for the 3d-3p and 4f-3d transitions based on the results of Storey (1994) but with transformation of radiative data to an intermediate coupling scheme limited to these transitions. All of the above calculations assumed that the three levels of the $O^{2+} \ ^3P$ ground term are populated according to their statistical weights, which is not usually the case in the conditions typically found in photoionised nebulae. In general, for any ionic level, if the ambient density is below the critical density for that level, its population will depart from a Boltzmann distribution and the population of all states formed by recombination on to that level will be affected. The result is that for recombination on to an ion with more than one level in the ground term, such as O^{2+} , the relative intensities of lines within all recombination multiplets will, in general, show some density dependence.

Ruiz *et al* (2003) investigated this effect empirically by considering the observed variation of the relative intensities

* E-mail: t.sochi@ucl.ac.uk

of the lines of O II multiplet V1 as a function of the electron number density derived from forbidden lines, mainly [Cl III]. This approach was further refined by Peimbert *et al* (2005) and Peimbert & Peimbert (2005). We compare these authors' results with our theoretical work in a subsequent section. Bastin (2006) and Bastin & Storey (2006) revised the calculation of Storey (1994) by describing the whole recombination process in intermediate coupling and including the distribution of population among the O^{2+} levels. They used an R-matrix scattering code (Berrington *et al* 1995) to compute oscillator strengths and photoionisation cross-sections, and hence recombination coefficients, for the low lying states of O^+ . McNabb *et al* (2013) presented various O II diagnostic line ratios derived from the theoretical results of Bastin (2006) and used them to analyse a large number of planetary nebula and H II region spectra.

In the present paper we use the techniques used by Bastin (2006) and Bastin & Storey (2006), and later also used by Fang *et al* (2011) for the recombination of N^{2+} , but with some modifications and improvements as described below. The results presented here differ, in some cases significantly, from those obtained by Bastin (2006). We return to this point in the relevant subsequent sections. We provide the resulting data in a text file containing a list of transitions between the lower states of O^+ and emission coefficients for these lines as a function of electron temperature and density and Case (A, B and C which will be explained later). We also provide a file containing recombination coefficients for the ground and metastable states of O^+ as functions of the same quantities. We also provide an interactive data server, in the form of a fortran 77 program, for mining the emission coefficient data and obtaining interpolated results for densities and temperatures between the explicitly computed values. More details will be given in the forthcoming sections.

As discussed briefly in Storey & Sochi (2015b), the current paper comes as part of a series of papers by the authors (Storey & Sochi 2013, 2014; Storey *et al* 2014; Storey & Sochi 2015a,b) aimed at providing the means to investigate the long-standing puzzle of the inconsistency between the results of elemental abundance and electron temperature as derived from the optical recombination lines (ORL) with those derived from the collisionally-excited lines (CEL). Several possible explanations for the discrepancy have been proposed including the proposal that the recombination lines are formed in regions of much lower temperature than implied by the CEL diagnostics. We therefore extend the calculation of recombination coefficients down to much lower electron temperatures (100 K) than is usually the case.

It has also been suggested that the free electron energy distribution may not be best described by a Maxwell-Boltzmann distribution (Nicholls *et al* 2012, 2013), so we plan to publish a further paper where recombination coefficients have been calculated with the free electron energies distributed according to the κ distribution suggested by these authors. We note, however, that the non-Maxwellian model at present has little theoretical (Ferland *et al* 2016) or observational (Storey & Sochi 2014; Zhang *et al* 2016) support.

The plan of the present paper is that in section 2 we give details of the calculation of the atomic parameters needed to calculate the population structure, including details of a

new R-matrix calculation of radiative properties. In section 3 we give details about the structure and contents of the data files and provide general instructions and explanations about how the data should be explored and used. Section 4 presents some comparisons between theory and observation and the paper is concluded in section 5 with general conclusions.

2 ATOMIC PARAMETERS FOR O^+

In this section we summarise the main features of the past and present calculations. We follow the methods used by Storey (1994), Bastin (2006), Bastin & Storey (2006) and Fang *et al* (2011) to compute the atomic parameters required to compute populations of the states of O^+ due to recombination processes. We refer the reader to those references for a fuller explanation.

2.1 The O^+ Term Scheme

The principal series of O^+ is $2s^2 2p^2 ({}^3P)nl$ which gives rise to doublet and quartet terms. Embedded within this series are the $2s^2 2p^2 ({}^1D)nl$, $2s^2 2p^2 ({}^1S)nl$, and $2s 2p^3 ({}^5S^o)nl$ series and terms of the $2s 2p^4$ configuration. Some of the members of these additional configurations lie above the first ionisation limit and can be a source of population *via* dielectronic recombination. In the calculation of Storey (1994) the states and radiative transitions of O^+ were described in LS -coupling but in this approximation several important processes could not be incorporated. To remedy this shortcoming, Bastin (2006) described the states of O^+ in a $J_c j$; J coupling scheme, where J_c is the total angular momentum quantum number of the O^{2+} state, j is that of the valence electron and J is the total for the O^+ state. This enabled two significant extensions to the work of Storey (1994): firstly, the populations of the ${}^3P_{J_c}$ levels of the O^{2+} recombining ion could be explicitly accounted for, and secondly the three series of Rydberg states converging on the ${}^3P_{J_c}$ levels could be treated separately. Figure 1 illustrates these states schematically. These Rydberg states are a channel for a dielectronic recombination process that operates at very low temperatures, below approximately 1000 K. In their calculation of N^{2+} recombination, Fang *et al* (2011) used the methods described by Bastin (2006) but modified the coupling scheme describing the O^+ states to a $J_c l(K)s; J$ scheme, where l and $s = 1/2$ are the orbital and spin angular momenta for the valence electron. In this scheme J_c is coupled with l to give the quantum number K , which in turn is coupled with s to give the total angular momentum quantum number J . This scheme has the advantage that it is the natural scheme for the high- l Rydberg states which appear in energetically close pairs characterised by $J = K \pm 1/2$. It is also the scheme used to describe the continuum states in the R-matrix electron scattering codes described below in Section 2.3. The experimental results for the energy levels of O^+ given by Martin *et al* (1993) were used here to assign K and J quantum numbers to O^+ states with $l > 2$. For states of lower l a transition to LS coupling takes place which is fully accounted for in the intermediate coupling R-matrix treatment of the bound states described below.

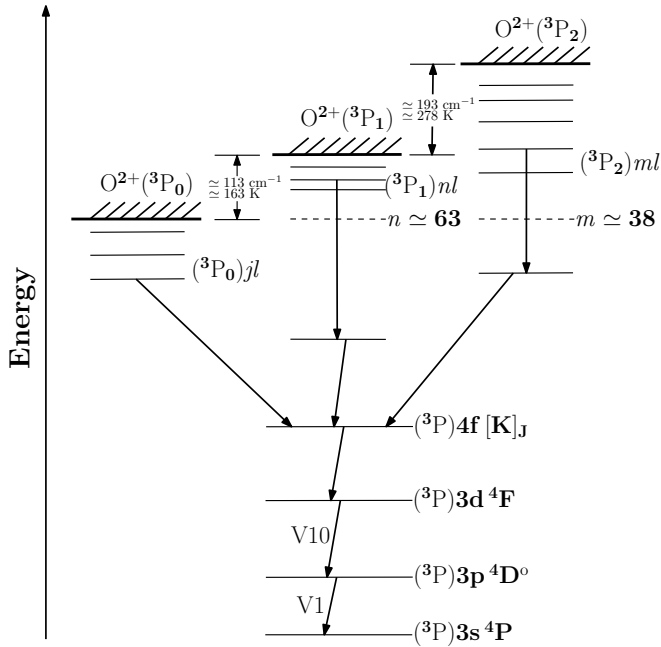


Figure 1. Schematic diagram of low-lying energy states of O^+ with some low-temperature dielectronic recombination transitions between fine-structure autoionising levels below the three lowest ionisation thresholds of O^{2+} : 3P_0 , 3P_1 and 3P_2 . Some multiplets arising from transitions between low-lying terms are also depicted schematically. The figure is qualitatively informative but is not drawn to scale.

2.2 O^+ Populations

Fang *et al* (2011) have described the calculation of the departure coefficients $b(J_c n l(K) s; J)$ defined by:

$$\frac{N(J_c n l(K) s; J)}{N_e N_+(S_c L_c; J_c)} = \left(\frac{N(J_c n l(K) s; J)}{N_e N_+(S_c L_c; J_c)} \right)_S b(J_c n l(K) s; J) \quad (1)$$

where $N(J_c n l(K) s; J)$, $N_+(S_c L_c; J_c)$ and N_e are the number densities of the O^+ state $J_c n l(K) s; J$, the O^{2+} state $S_c L_c; J_c$ and free electrons respectively and the subscript S signifies the ratio of the number densities given by the Saha-Boltzmann equation. There are three stages to the calculation as described originally by Storey (1994). To summarise, the first stage involves a calculation of $b(J_c n)$ for all $n \leq 1000$ for the $J_c = 0, 1, 2$ of the 3P ground term of O^{2+} . In addition to the collisional-radiative processes described by Hummer & Storey (1987) for hydrogen-like systems, autoionisation probabilities to and dielectronic capture probabilities from the available continua, averaged over l for each n , are incorporated. For $n > 1000$ we assume $b(J_c n) = 1$. In the second stage, departure coefficients $b(J_c n l(K) s; J)$ are calculated, still in a hydrogen-like approximation for all $n < n_l$, where n_l is the boundary above which l -changing collisions are sufficiently rapid that $b(nl) = b(n)$ is a good approximation. In the first two stages there are necessarily no radiative or collisional processes linking states of different J_c . The third and final stage deals with the departure coefficients for the states with $n < n_d$, where n_d is the boundary below which only radiative processes determine the populations, i.e. where collisional processes can be neglected.

2.3 R-matrix Calculation for $O^{2+} + e^-$

For the low-lying states of O^+ , the recombination coefficients were computed directly by integrating the photoionisation cross-sections, as obtained from an $O^{2+} + e^-$ R-matrix calculation in an intermediate coupling scheme using the Breit-Pauli approximation. Cross-sections were obtained for all the states with principal quantum numbers $n \leq 10$ and orbital angular momentum quantum numbers $l \leq 4$ in the principal series of O^+ plus all other states embedded among these. The calculation also provides bound state energies and oscillator strengths for use in the calculation of the O^+ level populations. The main codes used for the calculation are Autostructure¹ (Eissner *et al* 1974; Nussbaumer & Storey 1978; Badnell 2011) which was used to create the atomic target, and the UCL-Belfast-Strathclyde version of the R-matrix code² (Berrington *et al* 1995) to carry out the scattering calculations.

The Autostructure code was used to generate the target radial functions which are used as an input to the first stage of the R-matrix code. The radial data were produced using thirty-nine configurations synthesised from seven orbitals; three spectroscopic (1s, 2s and 2p) and four correlation orbitals ($\bar{3}s$, $\bar{3}p$, $\bar{3}d$ and $\bar{4}d$). This configuration basis was previously used by Storey *et al* (2014) in their work on the collision strengths of [O III] forbidden lines and is given in Table (1) of Storey *et al* (2014). The correlation orbitals are calculated in a Coulomb potential with central charge $8|\lambda_{nl}|$. An iterative optimisation variational procedure was employed to obtain the orbital scaling parameters, λ_{nl} , as supplied in Table (2) of Storey *et al* (2014).

In the R-matrix scattering calculations, 72 target terms, listed in Table (3) of Storey *et al* (2014), were used. For the 36 energetically lowest states, experimental energies obtained from Martin *et al* (1993), were used in the diagonal entries of the Hamiltonian in stage STG3 of the R-matrix code, instead of the theoretically computed values obtained from stage STG1, to provide accurate threshold energies and hence more accurate positions for resonances in the photoionisation cross-sections.

2.4 Energy Levels

The R-matrix calculation provides bound state energies for 674 levels with principal quantum number $n \leq 10$ and orbital angular momentum quantum number $l \leq 4$. The Hamiltonian used in the calculation of bound state energies includes electrostatic terms and one-body relativistic terms, i.e. the mass and Darwin relativistic energy shifts and the spin-orbit interaction. Two-body spin and orbit dependent terms are not included in this formulation. In Table 1 we compare the calculated ionisation energies with experiment for all terms up to the highest of the $2s^2 2p^2 3d$ electron configuration, 26 terms in all. The Table also shows the total fine-structure splitting of each term compared to the experimental value.

¹ See Badnell: Autostructure write-up on WWW. URL: amdpp.phys.strath.ac.uk/autos/ver/WRITEUP.

² See Badnell: R-matrix write-up on WWW. URL: amdpp.phys.strath.ac.uk/UK_RmaX/codes/serial/WRITEUP.

For states of the principal series, $2s^22p^2(^3P)3l$ the agreement between theory and experiment is excellent with a maximum difference of 0.9% and differences that are generally much less than 1%. There are larger differences for the members of the $(^1D)nl$ and $(^1S)nl$ series that are in this energy range, reaching a maximum of 1.1% and 2.8% respectively. For low l we can expect LS coupling to be a good approximation but to become increasingly inappropriate as l increases, independent of n . Liu *et al* (1995) discuss the coupling schemes that are appropriate for O^+ states and conclude that there is a partial breakdown of LS coupling for some of the $(^3P)3d$ states and that LS coupling is completely inappropriate for the $(^3P)4f$ levels. Departures from LS -coupling within a configuration $(^3P)nl$ depend, to a first approximation, on the inverse of the energy separation between states of the same total angular momentum J belonging to different terms, and the magnitude of the spin-orbit parameter for the orbital nl . The accuracy of the calculated spin-orbit parameter can be estimated by comparing the total fine-structure splitting of individual terms with experiment. Table 1 shows that the calculated and experimental total fine-structure splittings of the $(^3P)3l$ terms agree within 10%.

The large differences between theory and experiment for the very small fine-structure splittings of the $2s^22p^3\ ^2D^\circ$ and $\ ^2P^\circ$ terms arises because the spin-orbit parameter is zero for the half-filled $2p$ shell and the observed level separations are due to two-body fine-structure terms which are not included in our R-matrix formulation. In Table 2 we compare calculated and experimental energies for levels of the $2s^22p^2(^3P)4f$ and $5f$ configurations. These levels are no longer well represented in LS -coupling but appear as groups attached to each of the $\ ^3P_J$ parent levels. We show the statistically weighted mean energies of each group and the total fine-structure splitting of the group.

2.5 Bound-Bound and Bound-Free Radiative Data

The R-matrix calculation provides electric dipole oscillator strengths between all 674 bound states, which include spin-changing intercombination transitions. It also provides photoionisation cross-sections resolved by final target level from which recombination coefficients can be calculated. The energy mesh used to calculate the cross-sections is divided into two sections. From the energy of the $2s^22p^2\ ^3P_2$ target state to just below the $2s^22p^2\ ^1D_2$ threshold, a mesh of variable step is used. The step length is varied to ensure that resonance features in the cross-section, whose positions and widths have been previously determined, are well resolved. Details of this approach can be found in Kisielius *et al* (1998). This mesh terminates at effective quantum number, $\nu = 10$ relative to the $\ ^1D_2$ threshold and comprises 14244 energies. For higher energies the energy mesh between thresholds is defined by a fixed step, $\Delta\nu = 0.001$ in effective quantum number relative to the next threshold, giving rise to a further 11569 energies. For $\nu \geq 10$ relative to any threshold, the cross-section is obtained by Gaillitis averaging with the mesh determined by $\Delta\nu = 0.001$ relative to the next highest threshold. The mesh extends to just above the $2s\ 2p^3\ ^3D^\circ$ target state to an energy of 1.095 Rydberg. The calculations described by Bastin (2006) and Bastin & Storey (2006) were also based on an R-matrix calculation of

energy levels, oscillator strengths and photoionisation cross-sections, albeit with a simpler scattering target than the one used here. However, a re-examination of those photoionisation cross-sections shows that some of the cross-sections for the more highly excited states display non-physical features, such as unexpected oscillations and elevated continua. The results of the present calculation are therefore to be preferred.

For the 4f-3d and 3d-3p transition arrays we can compare our energies and branching ratios with those of Liu *et al* (1995) who used the atomic structure code SUPERSTRUCTURE (Eissner *et al* 1974; Nussbaumer & Storey 1978) to calculate energy levels and dipole matrix elements for these transition arrays in intermediate coupling. Liu *et al* (1995) made empirical corrections to the term and level energies and spin-orbit parameters to bring the energies close to experiment. In the R-matrix approach used here we can make corrections to the target energies but not to the final O^+ bound state energies. In Table 3 we compare individual level energies with experiment and with the results of Liu *et al* (1995) for the 3d and 4f configurations. The empirical adjustments made by Liu *et al* (1995) mean that they obtained better fine-structure splittings than those obtained here. In Tables 4 and 5 we compare the branching ratios for selected stronger components of the 3d-3p and 4f-3d transition arrays computed by Liu *et al* (1995) with the present work. For the larger branching ratios, greater than 0.1, there is general agreement between our results and those of Liu *et al* (1995) to within 3% for the 3d-3p transitions and to within 10% for the 4f-3d transitions. However, Liu *et al* (1995) point out that whereas the $\ ^4F$, $\ ^2P$ and $\ ^2D$ terms of the $2s^22p^23d$ configuration are well described by LS -coupling, the $\ ^4P$, $\ ^4D$ and $\ ^2F$ terms are not. In Table 5 we see that the largest differences between the present work and that of Liu *et al* (1995) occurs for transitions involving the $\ ^4D$ and $\ ^2F$ terms and in particular the $\ ^4D_{5/2}$ and $\ ^2F_{5/2}$ levels where the differences reach 40%. It is probable that the branching ratios calculated by Liu *et al* (1995) with empirical corrections to level energies and spin-orbit parameters are closer to reality than our *ab initio* results for these particular transitions. We note, however, that the predicted strength of the corresponding recombination lines also depends upon the relative populations of the $O^{2+}\ ^3P_J$ ground levels and these were assumed to be in proportion to statistical weights by Liu *et al* (1995). In the present calculation the $O^{2+}\ ^3P_J$ level populations were explicitly included and accounted for in the calculation of all the O^+ level populations. We return to this point below.

2.6 Autoionisation Probabilities

The calculation of the departure coefficients above the $\ ^3P_0$ ionisation limit and below the $\ ^3P_2$ limit requires, in addition to the usual collisional-radiative processes, rates for autoionisation and dielectronic capture. As shown in Figure 1, these additional processes apply for $n \geq 63$ in the $(^3P_1)nl$ series and $m \geq 38$ in the $(^3P_2)ml$ series. However, in an R-matrix calculation there is no allowance for the competition between autoionisation and radiative decay of the valence electron, so a simple integration of the photoionisation cross-section does not correctly treat the dielectronic recombination *via* these high n, m states. We therefore use AU-

TOSTRUCTURE (Eissner *et al* 1974; Nussbaumer & Storey 1978; Badnell 2011) to calculate the autoionisation probabilities for selected $n, m < 1000$ and $l \leq 30$ and to avoid duplication of the dielectronic component due to the (3P_1) nl and (3P_2) ml Rydberg states we begin the calculation of the R-matrix photoionisation cross-sections from the low-lying states at the energy of the $O^{2+} \ ^3P_2$ level. This provides the dielectronic contribution to the recombination, allowing for all the usual collisional-radiative processes but not the non-resonant or radiative recombination component, which we obtain by extrapolation of only the background photoionisation cross-section from above the 3P_2 threshold to the energy region between the 3P_0 and 3P_2 states.

3 RESULTS AND DISCUSSION

3.1 Structure and Contents of Data File

The O II recombination lines and their theoretically-computed emission coefficients (erg cm³ s⁻¹ per O²⁺ ion per electron) up to $n = 7$ are archived in a single file called “OIlines_ABC”, where ABC refers to the three “Cases” for which emission coefficients were calculated. Case A refers to the situation where all O⁺ radiative transitions are assumed optically thin. In Case B we assume that all radiative transitions terminating on the O⁺ $^4S_{3/2}^o$ ground level are sufficiently optically thick that the photons are re-absorbed on-the-spot in the same transition. Hence, these decays are excluded from the calculation of level populations. For Case C we also exclude decays to the O⁺ $^2D_{3/2}^o$ and $^2D_{5/2}^o$. This is a simple and relatively crude treatment of the effects of optical depth in resonance transitions but comparison with observations indicates that Case B is a much better approximation to reality in the majority of PNe than Case A or Case C. We briefly discuss the possible relevance of Case C in Section 4.

The “OIlines_ABC” file consists of two main sections preceded by a short header which consists of a general description of the file structure and the abbreviations used to label and explain the data blocks and their units. The structure of these sections is as follows:

1. The first section consists of 8889 indexed text lines corresponding to the provided 8889 O II transitions where each text line contains full identification of the corresponding transition by its upper and lower level as well as its wavelength in Å and other relevant atomic designations.
2. The second section consists of 8889 parts where each part corresponds to one transition as indexed above. Each part is made of three blocks where each block corresponds to one of the three Cases. Each one of these blocks is a rectangular array of emission coefficients of the indexed transition arranged in 25 rows, as a function of $\log_{10}(T_e[\text{K}])$ between 2.0–4.4 in steps of 0.1, and 16 columns as a function of $\log_{10}(N_e[\text{cm}^{-3}])$ between 2.0–5.0 in steps of 0.2. More details about the structure and contents of the data file are provided in the ReadMe file associating the distributed data set.

The data set distributed as part of the current work also includes a file called “OIImeta_ABC” containing the recombination coefficients (cm³ s⁻¹ per O²⁺ ion per electron) to the ground and meta-stable levels of O⁺ as functions of electron temperature and number density and Case (A, B and

C). The file contains 14 data blocks. The structure of the file is as follows:

1. A block for the effective recombination coefficients of the ground level $2s^22p^3 \ ^4S_{3/2}^o$ in Case A.
2. Four blocks for the effective recombination coefficients of the two levels $2s^22p^3 \ ^2D_{5/2}^o$ and $^2D_{3/2}^o$ each in Case A and B.
3. Six blocks for the effective recombination coefficients of the two levels $2s^22p^3 \ ^2P_{3/2}^o$ and $^2P_{1/2}^o$ each in Case A, B and C.
4. Three blocks for the total recombination coefficients, one block for each Case.

Each data block is structured as a function of electron temperature and number density in \log_{10} identical to the structure of the emission coefficient blocks in “OIlines_ABC” file, as described above. We note that direct recombination and all cascade contributions, excluding those between the metastable states themselves, are included in the calculation of the coefficients in the “OIImeta_ABC” file.

3.2 Data Mining

The data in the “OIlines_ABC” file can be excavated using the supplied fortran 77 interactive data server. This server reads the file and provides easy access to the lines and their emission coefficients at the desired T_e and N_e . When the required data are within the T_e and N_e ranges but are not at the grid points of T_e and N_e as described above, a 6-point Lagrange interpolation in temperature and density is used to provide the desired data. Two main options are offered by the data server: (1) Generate a line list, and (2) Extract emission coefficients for a user supplied list of lines in user specified conditions.

As for the first option, the server offers two choices: (1a) List all the 8889 lines (between 367.97 and 3.90713×10^7 Å), and (1b) Specify a wavelength range for the list of lines desired by the user. In each one of these cases (i.e. 1a and 1b) two files are generated that contain the list of lines where the lines in one of these files (named “OIIdata_list_eorder”) are ordered in decreasing emission coefficient and in the other file (named “OIIdata_list_worder”) in increasing order of wavelength; the full list in the latter file is preceded by a list of only the strongest lines in the required wavelength range. The emission coefficients in these files correspond to typical nebular conditions of $T_e = 10^4$ K and $N_e = 10^4$ cm⁻³.

Regarding the second option, the user is asked to supply a list of lines in a text file for which the data are required. The user then has the choice between (2a) Providing a list of $T_e[\text{K}]$ – $N_e[\text{cm}^{-3}]$ pairs in a file for which the data are needed, or (2b) Providing a range of $\log_{10}(T_e[\text{K}])$ and $\log_{10}(N_e[\text{cm}^{-3}])$ in a file defining a one- or two-dimensional grid for which the data are required. In all of these options (i.e. 1a, 1b, 2a and 2b) the user has the choice to have the data for Case A, B or C. More details about the data server and its input and output files are provided in the ReadMe file associating the distributed data and code.

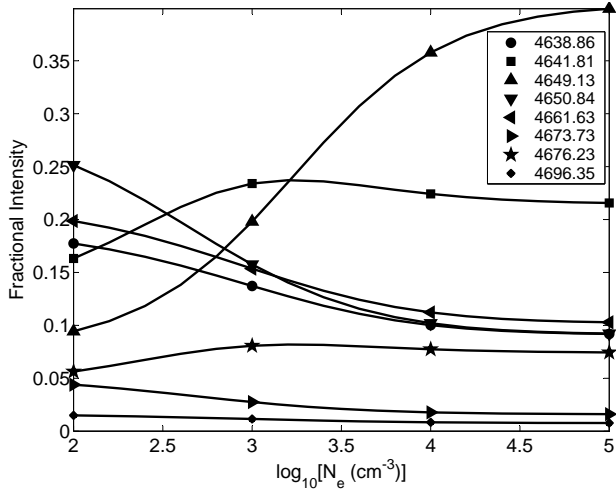


Figure 2. Computed fractional intensities of the eight transitions of the V1 multiplet of O II at $T_e = 10000$ K and in Case B as a function of $\log_{10}[N_e(\text{cm}^{-3})]$.

4 EXAMPLES OF COMPARISONS WITH OBSERVATIONS

4.1 Multiplet V1

The lines of O II multiplet V1 are among the brightest and most accessible spectroscopically. The relative intensities of the components of V1 depend upon the electron density *via* the distribution of population in the 3P_J ground levels of O^{2+} . This is illustrated in Figure 2 which shows the fractional intensities of the eight lines of V1 at a temperature of 10000 K. The relative populations of the 3P_J levels are approaching their local thermodynamic equilibrium values at $N_e = 10^5 \text{ cm}^{-3}$. At the higher densities the strongest component is the 4649.13 Å line which, arising from the $^4D_{7/2}^o$ level, is primarily formed by recombination from the $O^{2+} \ ^3P_2$ level at this temperature. The relative intensity of this component falls rapidly as the density and the population of the 3P_2 level fall. In their Figure 1, McNabb *et al* (2013) also present the fractional intensities of the eight lines of V1 over the same range of densities. Our results, which supersede those of McNabb *et al* (2013), are nevertheless in good agreement for this case.

In Figure 3 we show the fractional intensities for multiplet V1 at 1000 K. At this temperature the density variation of 4649.13 Å is much less marked than at 10000 K partly due to the effect of dielectronic recombination through the high- n Rydberg states converging on the 3P_1 and 3P_2 levels. Through this mechanism (3P_2) nl levels can be populated even at low electron density and, by radiative decays, eventually populate the upper level of the 4649.13 Å line. This process is only significant when the mean thermal energy of the free electrons is comparable to the 3P_J level separations. Very similar results were shown by McNabb *et al* (2013) in their Figure 1.

Baldwin *et al* (2000) and Esteban *et al* (2004) have published deep optical spectra of the Orion Nebula, M42. If we assume an electron temperature we can use the measured and computed relative intensities of the V1 lines to determine an electron density for the emitting regions. We adopt the temperature of 8320 K derived by Esteban *et al*

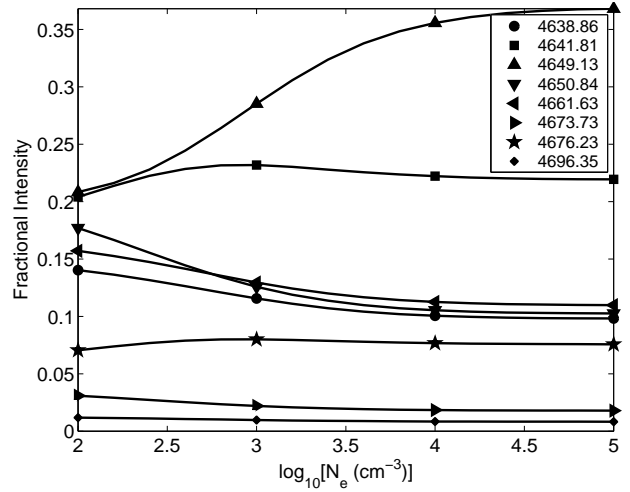


Figure 3. Computed fractional intensities of the eight transitions of the V1 multiplet of the O II at $T_e = 1000$ K and in Case B as a function of $\log_{10}[N_e(\text{cm}^{-3})]$.

(2004) for the higher ionisation species such as O^{2+} in M42 and locate the electron density that gives the best fit (least squares) between theory and observation for the seven lines of multiplet V1 for which measured intensities are available. In Figure 4 we show the theoretical fractional intensities plus the observed values from Baldwin *et al* (2000) and Esteban *et al* (2004) plotted at the best fit electron densities. The vertical error bars are the error estimates given by the authors and the horizontal error bar attached to the 4649.13 Å line is the one sigma uncertainty in the density derived from those observational errors. The agreement between theory and observation at the best fit densities is excellent. The derived densities of 7330 cm^{-3} and 4400 cm^{-3} can be compared with the value of 8900 cm^{-3} adopted for M42 by Esteban *et al* (2004) from a weighted average of forbidden line density diagnostics.

In Figure 5 we again use the observations of Baldwin *et al* (2000) and Esteban *et al* (2004) to derive electron densities which are the best fit to the seven observed lines of multiplet V2. The lines of V2 are weaker than those of V1 and the observational errors are consequently relatively larger, leading to larger uncertainties in the derived densities. Within the error bars there is reasonable agreement between the results derived from multiplets V1 and V2.

In Figure 6 we plot the intensity of V1 $\lambda 4649.13$ relative to the total V1 intensity as a function of electron number density. The results from the current work (CW) were calculated in Case B at 10000 K. We also show the effect on the ratio of switching off fine-structure dielectronic recombination (CW-NoFSDR). The solid curve (PP) shows the empirical results derived by Peimbert & Peimbert (2005) from the relationship between the observed values for a range of objects and the density derived from forbidden line ratios, in practice mainly from [Cl III]. Figure 6 also shows the results we obtain from the best fit of the relative intensities of all the observed lines of multiplet V1 to the theoretical relative intensities for three types of object: H II regions, PNe with low ADF, which we define as $ADF \leq 2.5$, and PNe with high ADF > 2.5 , where the ADF values were taken from Tsamis *et al* (2004), Table 9 (ORL/OPT for O^{2+}).

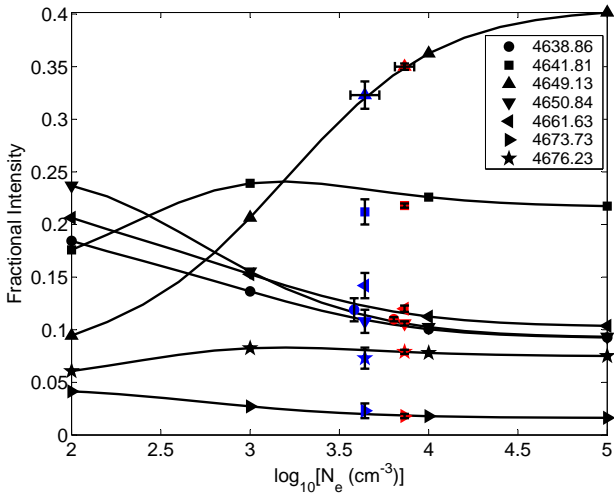


Figure 4. Computed fractional intensities in Case B of seven transitions of the V1 multiplet of the O II recombination lines at $T_e = 8320$ K as a function of $\log_{10}[N_e(\text{cm}^{-3})]$ with the observational intensities of the H II region Orion Nebula (M42) plotted at $N_e = 7330_{-350}^{+360} \text{ cm}^{-3}$ (red right) as obtained from Baldwin *et al* (2000) and at $N_e = 4400_{-740}^{+890} \text{ cm}^{-3}$ (blue left) as obtained from Esteban *et al* (2004). Some points are displaced horizontally to avoid overlapping.

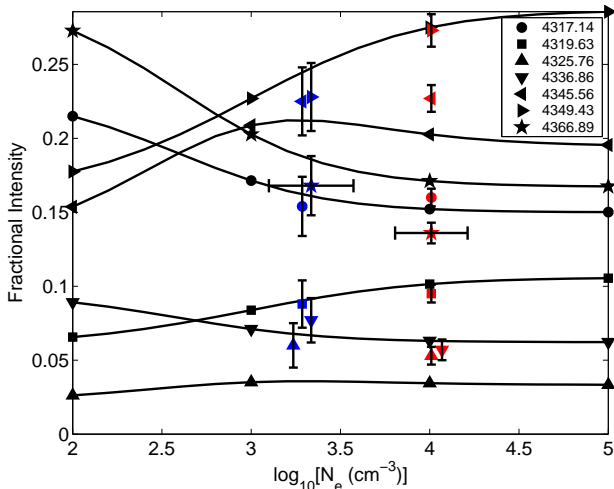


Figure 5. Computed fractional intensities in Case B of seven transitions of the V2 multiplet of the O II recombination lines at $T_e = 8320$ K as a function of $\log_{10}[N_e(\text{cm}^{-3})]$ with the observational intensities of the H II region Orion Nebula (M42) plotted at $N_e = 10210_{-4040}^{+12910} \text{ cm}^{-3}$ (red right) as obtained from Baldwin *et al* (2000) and at $N_e = 2170_{-940}^{+1640} \text{ cm}^{-3}$ (blue left) as obtained from Esteban *et al* (2004). Some points are displaced horizontally to avoid overlapping.

The densities resulting from the fits are given in numerical form in Table 6, which also lists the [O III] optical forbidden line temperature for each object. The theoretical values used in the fitting procedure were all calculated at 10000 K, which may not be appropriate for the high ADF PNe where there is some evidence that the recombination lines originate from a region at significantly lower temperature. As discussed above and shown in Figure 3 the variation of the

$\lambda 4649.13$ relative intensity with density is less pronounced at 1000 K than at 10000 K so that a given observed ratio would generally imply a lower electron density than those obtained from the fits at 10000 K and listed in Table 6. We note that the empirical curve of Peimbert & Peimbert (2005) is in good agreement with our theory except for low density objects, where the [Cl III] densities used by Peimbert & Peimbert (2005) tend to be lower than those derived here from the recombination line theory. There is therefore no clear indication from Figure 6 that the recombination lines are formed in a region of significantly different density to the [Cl III] forbidden lines, as might be expected if they originated from different physical regions.

The density variations of the V1 lines and the lines of other O II recombination multiplets result primarily from the density variations of the populations of the $\text{O}^{2+} \ ^3\text{P}_J$ levels. The critical density N_i^{crit} for a given level i , is given by:

$$N_i^{\text{crit}} = \sum_{k < i} A_{ik} / \sum_{k \neq i} q_{ik} \quad (2)$$

where A_{ik} are radiative transition probabilities and q_{ik} are rate coefficients for collisional excitation or de-excitation. If the ambient density is much greater than N_i^{crit} for a given level, the level population will approach the value given by the Boltzmann distribution. At 10^4 K the critical densities of the $^3\text{P}_1$ and $^3\text{P}_2$ levels are approximately 610 and 4350 cm^{-3} respectively but for the level populations to approach within 10% of Boltzmann values will require densities approximately 10 times the critical densities, i.e. 6100 and 43500 cm^{-3} . Typical PN (and H II region) densities are lower than this so we can conclude that the lines of all O II recombination multiplets will normally exhibit a significant dependence on density. Thus only in very high density nebulae can it be assumed that the $\text{O}^{2+} \ ^3\text{P}_J$ levels have a Boltzmann distribution of population and that the previous *LS*-coupling theoretical results (e.g. Storey (1994)) can be used to infer abundances from individual lines without knowledge of the electron density.

An additional consideration is that critical densities decrease with decreasing temperature, so that at 10^3 K for example, the values of $10 \times N_i^{\text{crit}}$ for the $^3\text{P}_1$ and $^3\text{P}_2$ levels of O^{2+} are 2500 and 15500 cm^{-3} respectively. These values are significantly lower than those at 10^4 K but not sufficiently low that a Boltzmann distribution can be safely assumed.

It is useful to apply the same argument to the recombination lines of N II and Ne II, where we find that $10 \times N_i^{\text{crit}}$ is 20500 cm^{-3} for the $^2\text{P}_{3/2}^o$ level of N^{2+} and 1.96×10^6 and $2.81 \times 10^5 \text{ cm}^{-3}$ for the $^3\text{P}_1$ and $^3\text{P}_0$ levels of Ne^{2+} . Therefore we anticipate that all recombination multiplets of N II and Ne II will show significant density dependence at nebular densities.

4.2 Density and Temperature Determinations

In the previous section we chose to use observations of M42 to initially illustrate the determination of electron density because there is broad agreement about the electron temperatures in M42 and H II regions generally. The same cannot be said about PNe where some models propose that recombination lines are formed in regions of much

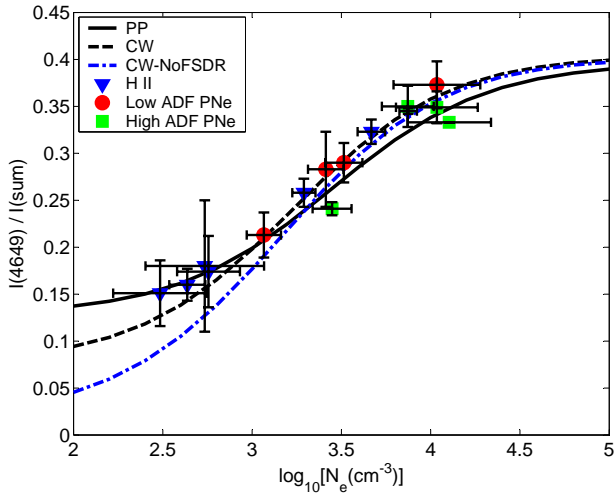


Figure 6. The intensity of $\lambda 4649.13$ relative to the total multiplet V1 intensity as a function of $\log_{10}[N_e(\text{cm}^{-3})]$ from Peimbert & Peimbert (2005) (PP), the current work (CW) and the current work neglecting fine-structure dielectronic recombination (CW-NoFSDR). The two curves showing the present work correspond to $T_e = 10000$ K in Case B. See Table 6 for information about the observational points.

lower temperature than those derived from forbidden line diagnostics. It is therefore of interest to seek diagnostics that determine both the density and the temperature of the regions where recombination lines are formed. In Figure 7 we plot a predominantly density sensitive line ratio $\lambda 4649.13/\lambda 4661.63$ against one which is mainly sensitive to temperature $\lambda 4649.13/\lambda 4089.29$, in Case B. The former pair of lines are from the V1 multiplet and the latter pair comprise the ratio of a V1 line with the strongest line from the 4f-3d transition array, $\lambda 4089.29$. In the latter case, both lines arise from the highest J of the transition array and hence depend strongly on the population of the 3P_2 ground level of O^{2+} , so that there is relatively little sensitivity to density in the ratio. Figure 2 of McNabb *et al* (2013) plots the same pair of ratios based on the earlier calculations of Bastin (2006), which shows some minor differences to our Figure 7, particularly in the values of the temperature sensitive $\lambda 4649.13/\lambda 4089.29$ ratio. As stated above, the earlier results contained defective photoionisation cross-sections for some states and are therefore superseded by the present work.

Peimbert & Peimbert (2013) have suggested that, in low resolution spectra, the intensity of the $\lambda 4089.29$ line may be affected by blending with a Si IV line at 4088.86\AA which, once corrected for, would potentially increase the observed $\lambda 4649.13/\lambda 4089.29$ ratio and result in deriving higher electron temperatures from this ratio. The Si IV $\lambda 4088.86$ line is part of a doublet with the other, weaker component at $\lambda 4116.10$, and a line at this wavelength has indeed been observed in M42 and several PNe (Peimbert & Peimbert 2013), although other identifications have been proposed. Thus caution should be exercised in deriving electron temperatures using a single ratio such as $\lambda 4649.13/\lambda 4089.29$.

Notwithstanding the possible blending issues, we show observational values for 23 objects including H II regions, low ADF PNe and high ADF PNe, defined as in the previous

section. The sources of the observational data are as follows. H II regions: Baldwin *et al* (2000), Tsamis *et al* (2003), Esteban *et al* (2004), García-Rojas *et al* (2004). Low ADF PNe: Hyung *et al* (2000), Tsamis *et al* (2003), García-Rojas *et al* (2015). High ADF PNe: Liu *et al* (1995), Liu *et al* (2000), Liu *et al* (2001), Tsamis *et al* (2003), Liu *et al* (2006), Fang & Liu (2011), McNabb *et al* (2016). The $\lambda 4089.29$ line which is used to constrain the temperature is a 4f-3d transition and is relatively weak. This is reflected in the large error bars on the $\lambda 4649.13/\lambda 4089.29$ ratio particularly for the H II regions while in the high ADF PNe, which exhibit stronger recombination lines, the error bars are relatively smaller. The three classes of objects broadly occupy different regions of the diagram. Most marked is the tendency for the high ADF PNe to cluster in the very low temperature region of the plot. The low ADF PNe, on the other hand, mainly occupy the region where temperatures are closer to 10000 K, although there are exceptions. The data for H II regions show a surprisingly large scatter in terms of temperature, which may be partially attributable to the intrinsic weakness of recombination lines when ADF factors are close to unity. We emphasise also that the theoretical results in Figure 7 were calculated in Case B which may not be the best approximation for H II regions which have large spatial extent and low ionisation. This may lead to sufficient population to build up in the $^2D_{3/2}^o$ and $^2D_{5/2}^o$ levels of O^+ for radiative transitions to these two levels to become optically thick and hence for Case C to be more appropriate than Case B.

5 CONCLUSIONS

We have calculated emission coefficients for recombination lines of O II over a range of electron temperatures and densities in Cases A, B and C, suitable for application to the spectra of photoionised nebulae. The calculation treats the important states in intermediate coupling and uses rates for bound-bound and bound-free radiative processes computed with the R-matrix method of electron scattering. The populations of the fine-structure levels of the ground term of O^{2+} are explicitly included, as is the effect of dielectronic recombination *via* high- n Rydberg states converging on these levels. To the best of our knowledge, these processes have not been included in any previous calculation of recombination coefficients for O II. Based on the above calculations, a large data set that comprises 8889 recombination lines with their emission coefficients as functions of electron temperature, number density and Case (A, B and C) accompanies this paper. An interactive data server, in the form of a fortran 77 code, is provided for the convenience of the users to explore the data and obtain Lagrange interpolated values between the explicitly provided ones. We also provide a data set of coefficients for recombination to the ground level and the four metastable levels of O^+ plus the total $O^{2+} + e^-$ recombination coefficients as functions of electron temperature and density and Case, for use in modelling the oxygen ionisation balance and calculating the recombination contribution to the excitation of the O II forbidden lines.

Comparison with observations showed that the lines of multiplet V1, the brightest of the O II recombination spectrum, provide a novel means of determining electron density, at least in those objects where the electron temperature is

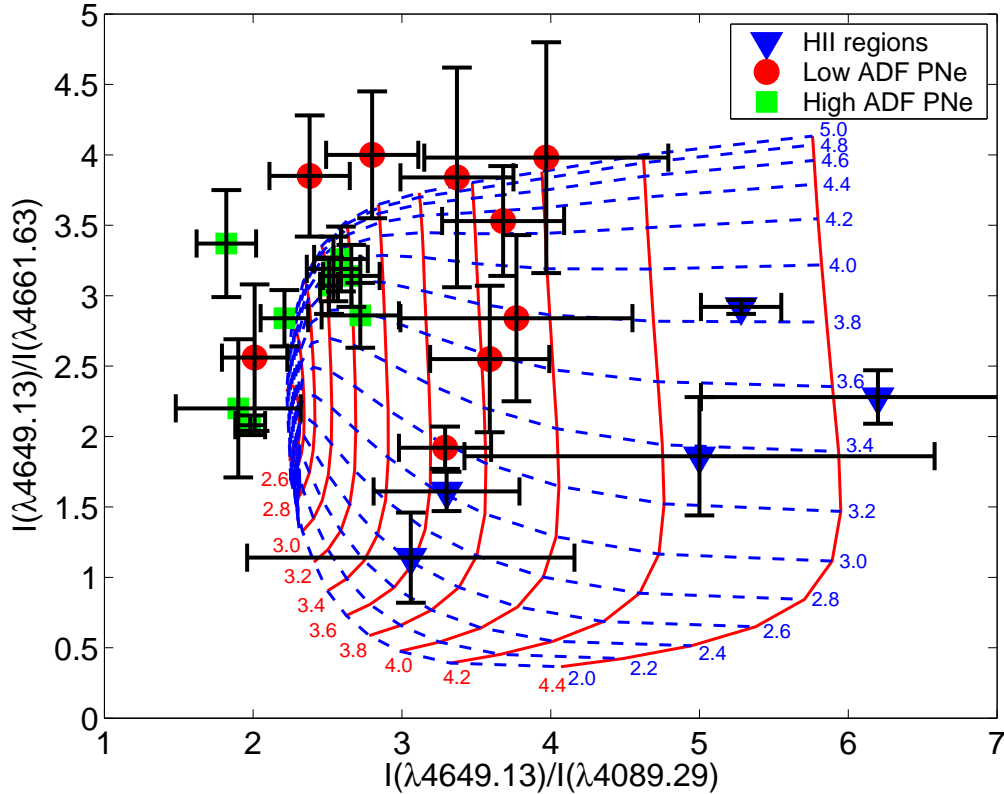


Figure 7. The ratio of our theoretical line intensities $I(\lambda 4649.13)/I(\lambda 4661.63)$ versus the ratio of our theoretical line intensities $I(\lambda 4649.13)/I(\lambda 4089.29)$ in Case B and as functions of $\log_{10}[T_e(\text{K})]$ (solid red) and $\log_{10}[N_e(\text{cm}^{-3})]$ (dashed blue). See the text for the sources of the observational points.

reasonably well known. We have also shown that there is good agreement between our calculated relative strengths of multiplet V1 as a function of electron density and empirical results derived from observations and CEL densities. The density dependence of the lines of the V1 multiplet at typical nebular densities is a result of these densities being below the critical densities for the ground levels of O^{2+} , and similar density dependence is therefore expected to appear in the components of all recombination multiplets of O II and in all ions where a similar situation prevails. Determining electron temperature from O II recombination lines is more problematic due to the relative weakness of the 4f-3d lines which, when compared to multiplet V1, show sensitivity to temperature. There does, however, seem to be evidence that, for the group of high ADF PNe considered here, the recombination lines are formed at a markedly lower temperature than is derived from CELs.

6 ACKNOWLEDGMENT

The authors would like to thank the reviewer Professor M. Peimbert for comments and corrections and for pointing out the possible blend of the $\lambda 4089.29$ line with a Si IV line. The work of PJS was supported in part by the STFC (grant ST/J000892/1).

7 STATEMENT

The complete data generated in this work can be obtained in electronic format with full precision from the Centre de Données astronomiques de Strasbourg (CDS) database. The fortran 77 data server is compiled and tested thoroughly using gfortran, f77, and Intel fortran compilers on Ubuntu 12.04 and Scientific Linux platforms. Representative sample results from all these compilers and on all those platforms are compared and found to be identical within the stated numerical accuracy.

REFERENCES

- Badnell N.R., 2011, *Comput. Phys. Commun.*, 182, 1528
- Baldwin J.A., Ferland G.J., Martin P.G., Corbin M.R., Cota S.A., Peterson B.M., Slettebak A., 1991, *ApJ*, 374, 580
- Baldwin J.A., Verner E.M., Verner D.A., Ferland G.J., Martin P.G., Korista K.T., Rubin R.H., 2000, *ApJS*, 129, 229
- Bastin R., 2006, PhD thesis, University College London
- Bastin R., Storey P.J., 2006, *Proceedings of the International Astronomical Union (Symposium S234)*, 369
- Berrington K.A., Eissner W.B., Norrington P.H., 1995, *Comp. Phys. Comm.*, 92, 290
- Eissner W., Jones M., Nussbaumer H., 1974, *Comp. Phys. Comm.*, 8, 270

- Esteban C., Peimbert M., García-Rojas J., Ruiz M.T., Peimbert A., Rodríguez M., 2004, *MNRAS*, 355, 229
- Esteban C., Bresolin F., Peimbert M., García-Rojas J., Peimbert A., Mesa-Delgado A., 2009, *ApJ*, 700, 654
- Fang X., Liu X.-W., 2011, *MNRAS*, 415, 181
- Fang X., Storey P.J., Liu X.-W., 2011, *A&A*, 530, A18
- Ferland G.J., Henney W.J., O'Dell C.R., Peimbert M., 2016, *Rev. Mex. Astron. Astr.*, 52, 261
- García-Rojas J., Esteban C., Peimbert M., Rodríguez M., Ruiz M.T., Peimbert A., 2004, *ApJS*, 153, 501
- García-Rojas J., Esteban C., Peimbert A., Peimbert M., Rodríguez M., Ruiz M.T., 2005, *MNRAS*, 362, 301
- García-Rojas J., Madonna S., Luridiana V., Sterling N.C., Morisset C., Delgado-Inglada G., Toribio San Cipriano L., 2015, *MNRAS*, 452, 2606
- Garnett D.R., Dinerstein H.L., 2001, *RevMexAA*, 10, 13
- Hummer D.G., Storey P.J., 1987, *MNRAS*, 224, 801
- Hyung S., Aller L.H., Feibelman W.A., Lee W.B., de Koter A., 2000, *MNRAS*, 318, 77
- Kisielius R., Storey P.J., Davey A.R., Neale L.T., 1998, *A&AS*, 133, 257
- Liu X.-W., Storey P.J., Barlow M.J., Clegg R.E.S., 1995, *MNRAS*, 272, 369
- Liu X.-W., Storey P.J., Barlow M.J., Danziger I.J., Cohen M., Bryce M., 2000, *MNRAS*, 312, 585
- Liu X.-W., Luo S.-G., Barlow M.J., Danziger I.J., Storey P.J., 2001, *MNRAS*, 327, 141
- Liu Y., Liu X.-W., Barlow M.J., Luo S.-G., 2004, *MNRAS*, 353, 1251
- Liu X.-W., Barlow M.J., Zhang Y., Bastin R.J., Storey P.J., 2006, *MNRAS*, 368, 1959
- Martin W.C., Kaufman V., Musgrove, A., 1993, *J. Phys. Chem. Ref. Data.*, 22, 1179
- McNabb I.A., Fang X., Liu X.-W., Bastin R., Storey P.J., 2013, *MNRAS*, 428, 3443
- McNabb I.A., Fang X., Liu X.-W., 2016, *MNRAS*, 461, 2818
- Mesa-Delgado A., Esteban C., 2010, *MNRAS*, 405, 2651
- Nicholls D.C., Dopita M.A., Sutherland R.S., 2012, *ApJ*, 752, 148
- Nicholls D.C., Dopita M.A., Sutherland R.S., Kewley L.J., Palay E., 2013, *ApJS*, 207, 1
- Nussbaumer H., Storey P.J., 1978, *A&A*, 64, 139
- Nussbaumer H., Storey P.J., 1984, *A&AS*, 56, 293
- Peimbert M., Storey P.J., Torres-Peimbert S., 1993, *ApJ*, 414, 626
- Peimbert A., 2003, *ApJ*, 584, 735
- Peimbert A., Peimbert M., 2005, *RevMexAA*, 23, 9
- Peimbert A., Peimbert M., Ruiz M.T., 2005, *ApJ*, 634, 1056
- Peimbert A., Peimbert M., 2013, *ApJ*, 778, 89
- Peimbert A., Peimbert M., Delgado-Inglada G., García-Rojas J., Peña M., 2014, *RevMexAA*, 50, 329
- Péquignot D., Petitjean P., Boisson C., 1991, *A&A*, 251, 680
- Robertson-Tessi M., Garnett D.R., 2005, *ApJS*, 157, 371
- Ruiz M.T., Peimbert A., Peimbert M., Esteban C., 2003, *ApJ*, 595, 247
- Smits D.P., 1991, *MNRAS*, 248, 193
- Storey P.J., 1994, *A&A*, 282, 999
- Storey P.J., Sochi T., 2013, *MNRAS*, 430, 599
- Storey P.J., Sochi T., 2014, *MNRAS*, 440, 2581
- Storey P.J., Sochi T., Badnell N.R., 2014, *MNRAS*, 441, 3028
- Storey P.J., Sochi T., 2015, *MNRAS*, 446, 1864
- Storey P.J., Sochi T., 2015, *MNRAS*, 449, 2974
- Tsamis Y.G., Barlow M.J., Liu X.-W., Danziger I.J., Storey P.J., 2003, *MNRAS*, 338, 687
- Tsamis Y.G., Barlow M.J., Liu X.-W., Danziger I.J., Storey P.J., 2003, *MNRAS*, 345, 186
- Tsamis Y.G., Barlow M.J., Liu X.-W., Storey P.J., Danziger I.J., 2004, *MNRAS*, 353, 953
- Wang W., Liu X.-W., 2007, *MNRAS*, 381, 669
- Wesson R., Liu X.-W., Barlow M.J., 2003, *MNRAS*, 340, 253
- Wesson R., Liu X.-W., Barlow M.J., 2005, *MNRAS*, 362, 424
- Zhang Y., Zhang B., Liu X.-W., 2016, *ApJ*, 817, 68

Table 1. The 26 lowest bound terms of the O⁺ ion, which include all levels up to the highest of the $1s^2 2s^2 2p^2 ({}^3P) 3d$ configuration in experimental energy order, and their experimental (E_{ex}) and theoretical (E_{th}) energies in Rydberg relative to the first ionisation limit ($1s^2 2s^2 2p^2 {}^3P_0$), as well as the total fine-structure splitting in cm^{-1} of each term experimentally (TSTE) and theoretically (TSTT). The column % E represents the percentage relative difference between the experimental and theoretical energies $\left[\frac{100(E_{\text{ex}} - E_{\text{th}})}{E_{\text{ex}}} \right]$ while the %S column represents a similar percentage for the splitting. The experimental energies are obtained from the NIST database (www.nist.gov) while the theoretical energies are obtained from the bound stage of the R-matrix code. The $1s^2$ core is suppressed from all configurations.

Index	Term	E_{ex}	E_{th}	% E	TSTE	TSTT	%S
1	$2s^2 2p^3 {}^4S^{\circ}$	-2.581409	-2.587200	-0.22	0.0	0.0	0.0
2	$2s^2 2p^3 {}^2D^{\circ}$	-2.337020	-2.333770	0.14	20.0	-8.8	143.9
3	$2s^2 2p^3 {}^2P^{\circ}$	-2.212625	-2.203115	0.43	2.0	-6.6	430.9
4	$2s 2p^4 {}^4P$	-1.488604	-1.487096	0.10	245.6	228.2	7.1
5	$2s 2p^4 {}^2D$	-1.068751	-1.052943	1.48	8.0	-6.6	181.9
6	$2s^2 2p^2 ({}^3P) 3s {}^4P$	-0.891730	-0.893485	-0.20	263.8	276.0	-4.6
7	$2s^2 2p^2 ({}^3P) 3s {}^2P$	-0.858863	-0.858604	0.03	180.0	191.2	-6.2
8	$2s 2p^4 {}^2S$	-0.797926	-0.769659	3.54	0.0	0.0	0.0
9	$2s^2 2p^2 ({}^3P) 3p {}^2S^{\circ}$	-0.722911	-0.725836	-0.40	0.0	0.0	0.0
10	$2s^2 2p^2 ({}^3P) 3p {}^4D^{\circ}$	-0.695903	-0.698399	-0.36	271.7	287.8	-5.9
11	$2s^2 2p^2 ({}^1D) 3s {}^2D$	-0.695301	-0.690584	0.68	1.0	-0.2	121.1
12	$2s^2 2p^2 ({}^3P) 3p {}^4P^{\circ}$	-0.681940	-0.684113	-0.32	138.1	148.7	-7.7
13	$2s^2 2p^2 ({}^3P) 3p {}^2D^{\circ}$	-0.652751	-0.652963	-0.03	190.6	196.3	-3.0
14	$2s^2 2p^2 ({}^3P) 3p {}^4S^{\circ}$	-0.648007	-0.649264	-0.19	0.0	0.0	0.0
15	$2s 2p^4 {}^2P$	-0.643687	-0.621974	3.37	168.4	162.1	3.8
16	$2s^2 2p^2 ({}^3P) 3p {}^2P^{\circ}$	-0.629299	-0.628628	0.11	59.8	65.0	-8.7
17	$2s^2 2p^2 ({}^1D) 3p {}^2F^{\circ}$	-0.496954	-0.492036	0.99	23.6	23.4	1.0
18	$2s^2 2p^2 ({}^1D) 3p {}^2D^{\circ}$	-0.485860	-0.481127	0.97	21.4	15.5	27.6
19	$2s^2 2p^2 ({}^1S) 3s {}^2S$	-0.479897	-0.466390	2.81	0.0	0.0	0.0
20	$2s^2 2p^2 ({}^3P) 3d {}^4F$	-0.472386	-0.471490	0.19	234.1	238.9	-2.0
21	$2s^2 2p^2 ({}^3P) 3d {}^4P$	-0.462644	-0.461378	0.27	139.8	135.0	3.4
22	$2s^2 2p^2 ({}^1D) 3p {}^2P^{\circ}$	-0.462528	-0.457352	1.12	46.6	45.8	1.9
23	$2s^2 2p^2 ({}^3P) 3d {}^4D$	-0.460410	-0.459278	0.25	42.2	38.7	8.2
24	$2s^2 2p^2 ({}^3P) 3d {}^2F$	-0.459102	-0.458015	0.24	162.9	160.9	1.3
25	$2s^2 2p^2 ({}^3P) 3d {}^2P$	-0.453929	-0.449836	0.90	114.1	112.9	1.0
26	$2s^2 2p^2 ({}^3P) 3d {}^2D$	-0.445033	-0.443454	0.35	51.8	48.6	6.2

Table 2. The mean energies and total fine-structure splittings of the levels of the configurations $1s^2 2s^2 2p^2 ({}^3P_J) 4f, 5f$ relative to the first ionisation limit. TSTE and TSTT are the experimental and theoretical total fine-structure splitting of each group of levels while %S is the percentage difference. Other aspects of the table are as explained in Table 1.

Configuration	E_{ex}	E_{th}	% E	TSTE	TSTT	%S
$2s^2 2p^2 ({}^3P_0) 4f$	-0.251329	-0.251097	0.09	1.4	1.9	36.0
$2s^2 2p^2 ({}^3P_1) 4f$	-0.250321	-0.250093	0.09	73.5	70.1	-4.6
$2s^2 2p^2 ({}^3P_2) 4f$	-0.247971	-0.247825	0.06	230.9	210.5	-8.8
$2s^2 2p^2 ({}^3P_0) 5f$	-0.160683	-0.160573	0.07	1.5	1.9	27.0
$2s^2 2p^2 ({}^3P_1) 5f$	-0.159670	-0.159557	0.06	49.1	46.6	-5.1
$2s^2 2p^2 ({}^3P_2) 5f$	-0.157735	-0.157653	0.05	111.8	100.0	-10.6

Table 3. Comparison of level energies in cm^{-1} within the $1s^2 2s^2 2p^2 ({}^3P)4f$ and $1s^2 2s^2 2p^2 ({}^3P)3d$ configurations between the experimental values (E_{ex}), the work of Liu *et al* (1995) (LSBC), and the current work (CW), where the given energies are relative to the lowest level in each configuration. The first three columns are reproduced from Table (3) of Liu *et al* (1995).

Level	E_{ex}	LSBC	CW
4f D[3] $^{\circ}_{5/2}$	0.0	0.0	0.0
4f D[3] $^{\circ}_{7/2}$	1.4	1.0	1.9
4f G[3] $^{\circ}_{5/2}$	66.2	66.3	67.4
4f G[3] $^{\circ}_{7/2}$	69.4	69.5	71.0
4f D[2] $^{\circ}_{3/2}$	122.7	122.7	124.2
4f D[2] $^{\circ}_{5/2}$	123.5	123.2	125.4
4f G[4] $^{\circ}_{9/2}$	137.7	137.7	135.2
4f G[4] $^{\circ}_{7/2}$	139.6	139.8	137.5
4f D[1] $^{\circ}_{3/2}$	222.3	221.9	227.3
4f D[1] $^{\circ}_{1/2}$	222.4	222.4	226.9
4f G[5] $^{\circ}_{11/2}$	287.5	287.5	286.8
4f G[5] $^{\circ}_{9/2}$	293.6	294.2	293.7
4f F[2] $^{\circ}_{3/2}$	393.7	393.3	378.0
4f F[2] $^{\circ}_{5/2}$	397.8	397.3	382.8
4f F[3] $^{\circ}_{7/2}$	433.3	432.9	417.5
4f F[3] $^{\circ}_{5/2}$	435.8	435.4	417.5
4f F[4] $^{\circ}_{9/2}$	446.1	445.8	429.5
4f F[4] $^{\circ}_{7/2}$	453.3	452.8	437.7
3d ${}^4F_{3/2}$	0.0	0.0	0.0
3d ${}^4F_{5/2}$	53.9	54.5	55.3
3d ${}^4F_{7/2}$	131.8	133.0	134.8
3d ${}^4F_{9/2}$	234.1	236.1	238.9
3d ${}^4P_{5/2}$	1166.6	1158.6	1211.5
3d ${}^4P_{3/2}$	1239.8	1234.2	1282.3
3d ${}^4P_{1/2}$	1306.4	1303.5	1346.4
3d ${}^4D_{1/2}$	1415.5	1415.2	1447.6
3d ${}^4D_{3/2}$	1449.9	1449.6	1481.0
3d ${}^4D_{5/2}$	1451.4	1453.0	1478.7
3d ${}^4D_{7/2}$	1457.7	1460.9	1486.4
3d ${}^2F_{5/2}$	1500.2	1502.0	1525.3
3d ${}^2F_{7/2}$	1663.1	1665.6	1686.2
3d ${}^2P_{3/2}$	2134.4	2131.4	2488.5
3d ${}^2P_{1/2}$	2248.4	2260.5	2601.4
3d ${}^2D_{3/2}$	3106.7	3105.4	3186.6
3d ${}^2D_{5/2}$	3158.5	3161.7	3235.2

Table 4. Branching ratios for the strongest 3d-3p transitions in Case B as obtained by Liu *et al* (1995) (LSBC) and the current work (CW) where λ is the air wavelength.

Transition	$\lambda[\text{\AA}]$	LSBC	CW
$^4F_{9/2} - ^4D_{7/2}^o$	4075.86	1.000	1.000
$^4F_{7/2} - ^4D_{7/2}^o$	4092.93	0.119	0.119
$^4F_{7/2} - ^4D_{5/2}^o$	4072.15	0.864	0.862
$^4F_{5/2} - ^4D_{7/2}^o$	4106.02	0.007	0.007
$^4F_{5/2} - ^4D_{5/2}^o$	4085.12	0.216	0.216
$^4F_{5/2} - ^4D_{3/2}^o$	4069.89	0.761	0.759
$^4F_{3/2} - ^4D_{5/2}^o$	4094.14	0.016	0.017
$^4F_{3/2} - ^4D_{3/2}^o$	4078.84	0.264	0.264
$^4F_{3/2} - ^4D_{1/2}^o$	4069.62	0.715	0.715
$^4D_{7/2} - ^4D_{7/2}^o$	3882.19	0.137	0.134
$^4D_{7/2} - ^4D_{5/2}^o$	3863.50	0.016	0.016
$^4D_{7/2} - ^2D_{5/2}^o$	4751.28	0.021	0.021
$^4D_{7/2} - ^4P_{5/2}^o$	4119.22	0.378	0.370
$^4P_{5/2} - ^4D_{5/2}^o$	3907.46	0.054	0.059
$^4P_{5/2} - ^4P_{5/2}^o$	4169.23	0.153	0.133
$^4P_{5/2} - ^4D_{3/2}^o$	3893.52	0.013	0.014
$^4P_{5/2} - ^4P_{3/2}^o$	4153.30	0.449	0.458
$^4P_{5/2} - ^4S_{3/2}^o$	4924.53	0.289	0.283

Table 5. Branching ratios for the strongest 4f-3d transitions. All other aspects are as for Table 4.

Transition	$\lambda[\text{\AA}]$	LSBC	CW
G[5] _{11/2} ^o - ⁴ F _{9/2}	4089.29	1.000	0.999
G[5] _{9/2} ^o - ⁴ F _{9/2}	4088.27	0.023	0.023
G[5] _{9/2} ^o - ⁴ F _{7/2}	4071.24	0.204	0.204
G[5] _{9/2} ^o - ² F _{7/2}	4342.01	0.702	0.695
G[5] _{9/2} ^o - ⁴ D _{7/2}	4303.61	0.072	0.076
G[4] _{9/2} ^o - ⁴ F _{9/2}	4114.51	0.019	0.017
G[4] _{9/2} ^o - ⁴ F _{7/2}	4097.26	0.735	0.731
G[4] _{9/2} ^o - ² F _{7/2}	4371.62	0.125	0.118
G[4] _{9/2} ^o - ⁴ D _{7/2}	4332.70	0.121	0.133
G[4] _{7/2} ^o - ⁴ F _{7/2}	4096.94	0.046	0.044
G[4] _{7/2} ^o - ⁴ F _{5/2}	4083.90	0.428	0.423
G[4] _{7/2} ^o - ² F _{5/2}	4340.33	0.354	0.320
G[4] _{7/2} ^o - ⁴ D _{5/2}	4331.17	0.123	0.159
G[4] _{7/2} ^o - ² D _{5/2}	4677.07	0.046	0.052
G[3] _{7/2} ^o - ⁴ F _{7/2}	4108.76	0.054	0.054
G[3] _{7/2} ^o - ⁴ D _{7/2}	4345.56	0.050	0.052
G[3] _{7/2} ^o - ⁴ F _{5/2}	4095.64	0.296	0.280
G[3] _{7/2} ^o - ² F _{5/2}	4353.59	0.162	0.117
G[3] _{7/2} ^o - ⁴ D _{5/2}	4344.38	0.189	0.221
G[3] _{7/2} ^o - ⁴ P _{5/2}	4291.26	0.246	0.273
F[4] _{9/2} ^o - ⁴ F _{9/2}	4062.93	0.150	0.152
F[4] _{9/2} ^o - ⁴ F _{7/2}	4046.12	0.015	0.019
F[4] _{9/2} ^o - ² F _{7/2}	4313.44	0.153	0.166
F[4] _{9/2} ^o - ⁴ D _{7/2}	4275.55	0.681	0.662
F[4] _{7/2} ^o - ⁴ F _{7/2}	4044.95	0.024	0.022
F[4] _{7/2} ^o - ² F _{7/2}	4312.11	0.098	0.103
F[4] _{7/2} ^o - ⁴ D _{7/2}	4274.25	0.035	0.030
F[4] _{7/2} ^o - ⁴ F _{5/2}	4032.24	0.017	0.019
F[4] _{7/2} ^o - ⁴ D _{5/2}	4273.10	0.081	0.070
F[4] _{7/2} ^o - ² D _{5/2}	4609.43	0.725	0.733
F[4] _{7/2} ^o - ⁴ P _{5/2}	4221.70	0.017	0.020
F[3] _{7/2} ^o - ⁴ F _{9/2}	4065.05	0.016	0.016
F[3] _{7/2} ^o - ⁴ F _{7/2}	4048.22	0.094	0.099
F[3] _{7/2} ^o - ² F _{7/2}	4315.83	0.046	0.044
F[3] _{7/2} ^o - ⁴ D _{7/2}	4277.90	0.154	0.159
F[3] _{7/2} ^o - ² F _{5/2}	4285.68	0.298	0.354
F[3] _{7/2} ^o - ⁴ D _{5/2}	4276.75	0.314	0.265
F[3] _{7/2} ^o - ² D _{5/2}	4613.68	0.074	0.059
D[3] _{7/2} ^o - ⁴ D _{7/2}	4358.44	0.026	0.021
D[3] _{7/2} ^o - ⁴ F _{5/2}	4107.09	0.173	0.190
D[3] _{7/2} ^o - ² F _{5/2}	4366.53	0.050	0.047
D[3] _{7/2} ^o - ⁴ D _{5/2}	4357.25	0.079	0.091
D[3] _{7/2} ^o - ² D _{5/2}	4707.50	0.014	0.016
D[3] _{7/2} ^o - ⁴ P _{5/2}	4303.82	0.652	0.630

Table 6. The intensity ratios I_{4649}/I_{sum} and the electron densities $N_e(\text{O II})$ as obtained from the present work for the observational data of Figure 6 where in the 2nd column H stands for H II regions, PL for PNe with low ADF and PH for PNe with high ADF. The line intensities, [Cl III] densities and [O III] temperatures are taken from the cited references. The electron densities N_e in the 4th and 5th columns are in cm^{-3} .

Object	Type	I_{4649}/I_{sum}	$N_e(\text{O II})$	$N_e([\text{Cl III}])$	$T_e([\text{O III}])$	Reference
30 Doradus	H	0.160±0.017	430 ⁺¹¹⁰ ₋₉₀	270 ⁺²⁵⁰ ₋₂₃₀	9950±60	1
30 Doradus	H	0.174±0.038	570 ⁺²⁸⁰ ₋₁₉₀	480	10100	2
M42	H	0.345±0.003	7480 ⁺¹⁶⁰⁰ ₋₁₃₂₀		9300	3
M42	H	0.323±0.013	4660 ⁺⁹⁰⁰ ₋₇₆₀	9400 ⁺¹²⁰⁰ ₋₇₀₀	8300±40	4
NGC 3576	H	0.258±0.015	1950 ⁺³¹⁰ ₋₂₇₀	3500 ⁺⁹⁰⁰ ₋₇₀₀	8500±50	5
S311	H	0.180±0.070	540 ⁺⁶²⁰ ₋₂₉₀	550 ⁺³⁵⁰ ₋₅₅₀	9000±200	6
NGC 604	H	0.151±0.035	310 ⁺²⁵⁴ ₋₁₄₀	100 ⁺¹⁰⁰ ₋₅₀	8150±160	7
NGC 5315	PL	0.373±0.025	10840 ⁺⁸¹³⁰ ₋₁₀₈₀	22825	8850	8
NGC 3132	PL	0.213±0.024	1160 ⁺²⁹⁰ ₋₂₃₀	720	9530	9
NGC 3242	PL	0.283±0.040	2590 ⁺⁶⁷⁰ ₋₅₃₀	1200	11700	9
NGC 3918	PL	0.290±0.021	3270 ⁺⁸⁸⁰ ₋₇₀₀	5500	12600	9
NGC 2022	PH	0.350±0.022	7450 ⁺²⁹⁵⁰ ₋₂₁₀	850	15000	9
NGC 6153	PH	0.333	12710 ⁺⁹⁰⁷⁰ ₋₅₃₀₀	3830	9110	10
M1-42	PH	0.241±0.007	2810 ⁺⁸⁰⁰ ₋₆₂₀	1580 ⁺²⁰⁰ ₋₄₆₀	8900±300	11
NGC 7009	PH	0.349±0.017	10840 ⁺⁷⁵³⁰ ₋₄₄₄₀	3600	9810	12

References: (1) Peimbert (2003) (2) Tsamis *et al* (2003) (3) Baldwin *et al* (1991, 2000) (4) Esteban *et al* (2004) (5) García-Rojas *et al* (2004) (6) García-Rojas *et al* (2005) (7) Esteban *et al* (2009) (8) Ruiz *et al* (2003) (9) Tsamis *et al* (2003) (10) Liu *et al* (2000) (11) McNabb *et al* (2016) (12) Fang & Liu (2011).